

ON PLASMA DIAGNOSTICS

D.M. Benenson and H.S. Kwok

Department of Electrical and Computer Engineering
State University of New York at Buffalo, Amherst, New York 14226 U.S.A.

Abstract - An overview is given of four diagnostic methods applicable to the determination of the local temperature (and particle density) and velocity fields in plasmas: spectroscopy, laser-induced fluorescence, interferometry, and laser velocimetry.

INTRODUCTION

Plasmas are operated over a wide range of conditions. Pressures can range from near-vacuum to tens of bars; current from a few amperes to around 100kA; flow velocity from zero to several thousand m/s (flows can exhibit laminar or turbulent characteristics, be strongly accelerating (as in a converging-diverging nozzle) or decelerating (through shock waves)). With these varied cases, temperature can range from a fraction of an eV to the order of 10eV, with associated ranges in particle densities and plasma composition. Nonequilibrium effects may play important roles in both switching and processing applications. Given the wide range available within one area (e.g., switching), it is important to apply several diagnostic methods so that results can be verified by (preferably) independent means, as well as to extend the range of observation. In the present paper a brief review is given of four methods - spectroscopy, laser-induced fluorescence, interferometry, and laser velocimetry. The first three techniques address temperature (and, thereby, particle density) while laser velocimetry is directed to studies of the flow field.

SPECTROSCOPY

Classical spectroscopy continues to provide an effective means for the determination of temperature (and particle density) through, say, the observation of line and continuum radiation. The line emission coefficient (integrated over the line profile) can be expressed

$$\epsilon_L = \epsilon_{mn} = \frac{hc}{4\pi\lambda_{mn}} N_m A_{mn} \quad (1)$$

(where A_{mn} = transition probability between upper level m and lower level n , c = speed of light, h = Planck's constant, N_m = particle density in level m , λ_{mn} = wavelength of the transition.) Presuming the existence of local thermal equilibrium (LTE) (1) and making use of the Boltzmann factors, Eqn. (1) becomes

$$\epsilon_L = \epsilon_{mn} = \frac{1}{4\pi} \frac{hc}{\lambda_{mn}} A_{mn} \frac{N_a g_m}{Z_a} \exp(-E_m/kT) \quad (2)$$

(where E_m = energy of level m , g_m = statistical weight of level m , k = Boltzmann constant, N_a = neutral atom density, T = temperature, Z_a = partition function for neutrals.)

The continuum emission coefficient is expressed as

$$\epsilon_c = \epsilon_{ff} + \epsilon_{fb} \quad (3)$$

(where ϵ_{fb} = emission coefficient for free-bound (recombination) radiation, ϵ_{ff} = emission coefficient for free-free (bremsstrahlung radiation). One expression, of several put forward (2), is the Kramers-Unsold relation

$$\epsilon_c = 5.44 \times 10^{-46} N_e N_i T^{-1/2} Z_{eff}^2 \bar{G} \quad (4)$$

(where \bar{G} = mean Gaunt factor, N_e = electron number density, N_i = ion number density, T =

temperature, Z_{eff}^2 = effective nuclear charge.)

With the assumption of LTE, particle densities become functions of two thermodynamic variables, say temperature and pressure. [Electron density may be determined independently through line broadening measurements (1,3) via Stark profiles.]

It should be recalled that observation of the radiation generally is along a line of sight across the plasma column. Consequently, at a given axial station, z , the observer records the integrated intensity, I

$$I(x; z) = \int \epsilon(x, y) dy \quad (5)$$

(where $I(x; z)$ = integrated intensity (for a given axial station, z) measured at chordwise station, x , (x, y, z) = rectangular coordinates.) In order to determine the spatial distribution of temperature through Eqns. (2) and/or (4), Eqn. (5) must be inverted to obtain the local values of emission coefficient. For the case of the cylindrical plasma, the inversion typically is accomplished using the Abel transform (1). In the event the column does not exhibit such symmetry (e.g., the cross-flow plasma), alternate, more general methods have been developed and applied (4-6).

With the local distribution of emission coefficients obtained through, say, Eqn. (5), local temperature may be determined upon calibration of the optical system. Absolute calibration of the optical system leads to the need of but a single data input to either Eqn. (2) or Eqn. (4) - e.g., radiation from one line. With relative calibration, a minimum of two inputs is required, such as two lines, or one line and one continuum. The use of multiple lines, to form the Boltzmann plot, is illustrated by taking the logarithm of both sides of Eqn. (2)

$$\ln \left[\frac{\epsilon_{mn} \lambda_{mn}}{g_m A_{mn}} \right] = - \frac{E_m}{kT} + \ln \left[\frac{hc N_a}{4\pi Z_a} \right] \quad (6)$$

By measuring the emission coefficients of a number of lines, a plot of $\ln[\epsilon_{mn} \lambda_{mn} / g_m A_{mn}]$ vs. E_m : (1) yields a straight line of slope $-1/kT$, from which the temperature can be determined and (2) forms, at the intercept, $\ln[hc N_a / 4 Z_a]$, from which N_a may be found. An example is shown in Fig. 1.

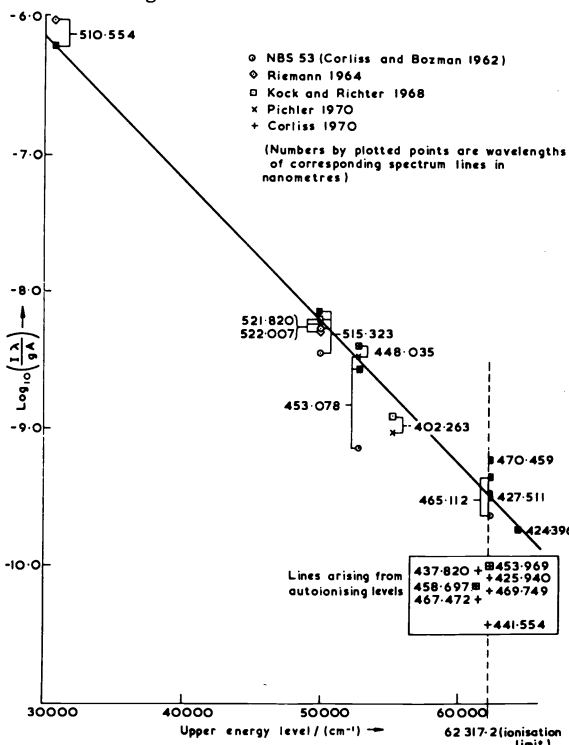


Fig. 1. Boltzmann plot for determination of temperature (Ref. 7).

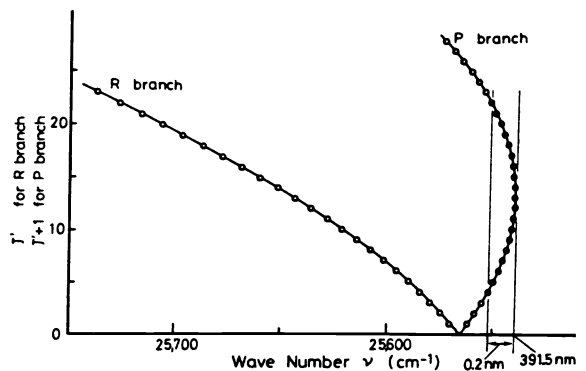


Fig. 2. Fortrat parabolas for the rotational band spectrum due to the $(0,0)$ vibrational transition of the $B^2\Sigma_u^+ \rightarrow X^2\Sigma_g^+$ electronic system of N_2^+ (Ref. 9).

For many gases, sufficient radiation exists so that, say, line emission methods enable the measurement of temperatures to as low as about 7,000K (8). With molecular gases, electronic transitions may be used to obtain temperatures down to around 4,000K (8). The emission coefficient, ϵ , of a rotational line can be expressed (7)

$$\epsilon = \frac{h c \sigma}{4 \pi} A_{n''v''K''J''}^{n'v'K'J'} N(n',v',K'J'p) \quad (7)$$

(where $()' = ()$ in the initial level, $()'' = ()$ in the final level, $A_{n''v''K''J''}^{n'v'K'J'}$ = transition probability, N = molecular density in initial level, (n,v,K,J) = electronic, vibrational, total angular momentum, rotational quantum numbers, respectively, p = parity, σ = wave number.) For a gas in LTE, Eqn. (7) becomes ((7), (9), (10))

$$\epsilon = C v^4 \frac{N}{Z} S_{J''} \exp[E_r(J'') + E_{v''} + E_{e''})/kT] \quad (8)$$

(where C = coefficient, including constants and magnitude of the dipole moment of the molecule, $E_{e''}$ = electronic energy, E_r = rotational energy in upper level, $E_{v''}$ = vibrational energy in upper level, J'' = rotational quantum number of the upper level, k = Boltzmann constant, N = number density of molecule, $S_{J''}$ = intensity factor, T = temperature, Z = internal partition function.)

Equations(7) and (8) lead, then, to a rich spectrum in comparison to that found with line radiation. The intervals between rotational lines forming a band spectrum typically are so narrow that their resolution requires spectrometers of high resolving power. By integrating over the rotational lines around the band head (and in the region where the lines of various branches do not overlap), however, this difficulty can be overcome and spectrometers of modest resolving power can be employed to determine temperatures. The latter approach has been developed (7,9) and applied (9) to determine the temperature distribution within an air plasma. Shown in Fig. 2 are the two branches appropriate to the (0,0) vibrational transition of the $B^2\Sigma_u^+ \rightarrow X^2\Sigma_g^+$ electronic system of N_2^+ . The exit slit width of the spectrometer was set at 0.2nm, over the wavelength region containing nineteen rotational lines about the band head in the P branch. Note that none of these lines overlaps those within the R branch. The temperature dependence of the integrated emission coefficients of the lines, normalized to the peak value (at 8900K), is shown in Fig. 3. Radial distributions of temperature for air arcs of various currents are shown in Fig. 4.

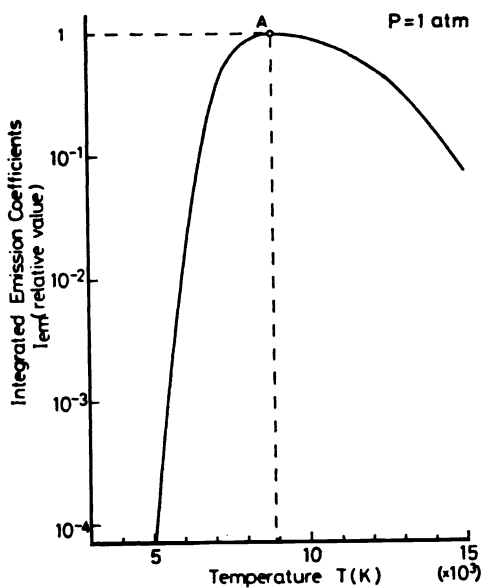


Fig. 3. Temperature dependence of the integrated emission coefficients of the selected nineteen lines in the P branch (Ref. 9).

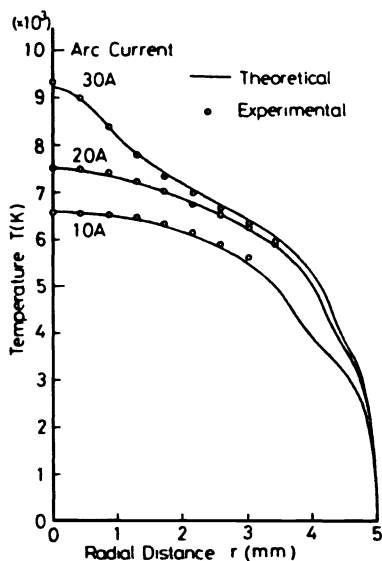


Fig. 4. Radial distributions of temperature in an atmospheric, wall stabilized air arc within a 10mm diameter channel (Ref. 9).

For temperatures below about 4,000K, radiation becomes too small to serve as a diagnostic (8). Thermocouples may be employed in this low temperature regime. Even though local data may be obtained, it should be noted that the technique is invasive. Further, owing to their thermal inertia, thermocouples are restricted to plasmas that are static or that change but slowly with time.

Dynamic plasmas (e.g., those found in circuit interruption devices), require appropriately rapid data acquisition techniques. One such method uses a high speed rotating mirror (11,12) to scan (or traverse) the image of the arc past the entrance slits of a spectrometer at speeds

to about 3mm/ μ s. Appropriate electronic synchronization permits the data to be obtained at known times during the transient. Examples of the timewise dependence of centerline temperature, and of the radial distribution of temperature at various times, during respective transients, are shown in Figs. 5 and 6, respectively.

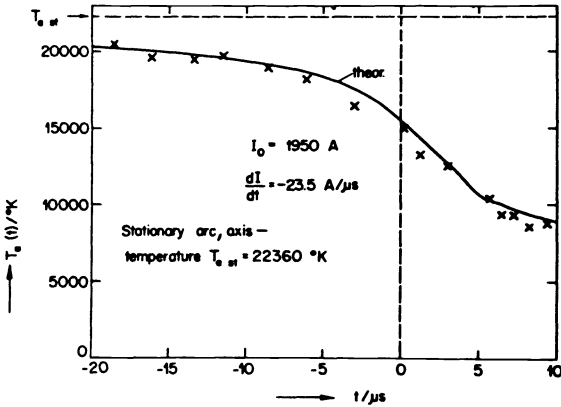


Fig. 5. Timewise dependence of centerline temperature in the stagnation region and near current zero of a 23 bar nitrogen plasma, Initial current = 2kA, $dI/dt = 24A/\mu s$. (Ref. 11).

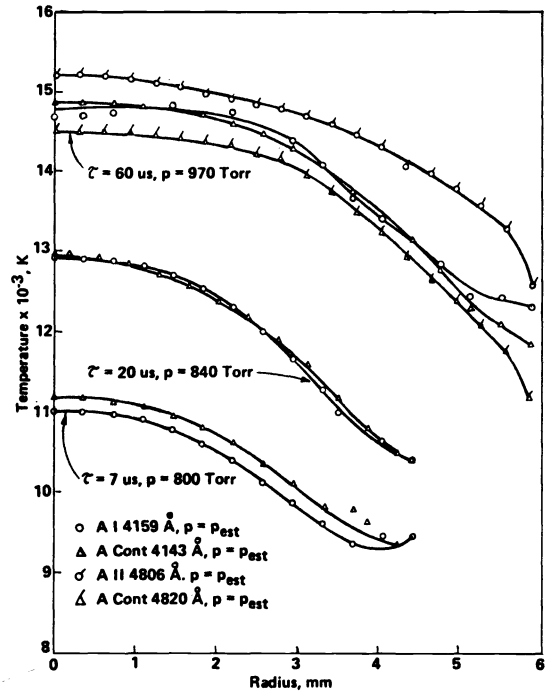


Fig. 6. Radial distributions of temperature at various times into the transient of a step voltage pulsed laminar, atmospheric argon arc (Ref. 12).

Many plasmas exhibit (hydrodynamic) turbulence whether in steady-state (13,14) or dynamic operation (11). Even under such unfavorable conditions spectroscopic methods can, in principle (15), be employed to determine radial distributions of temperature and the mean-square fluctuations. An extension (14) of Ref. 15 was formulated so as to reduce the totality of equations, the number of experimental inputs, and the complexity and associated errors of experiments. Expressions for the time-averaged line and continuum emission coefficients and their mean-square fluctuations were obtained in the form

$$\langle \epsilon_L \rangle = \langle \epsilon_{L_0} \rangle [1 + f_1 \langle \delta^2 T \rangle / \langle T \rangle^2] \quad (9)$$

$$\langle \epsilon_c \rangle = \langle \epsilon_{c_0} \rangle [1 + f_2 \langle \delta^2 T \rangle / \langle T \rangle^2] \quad (10)$$

$$\langle \delta^2 \epsilon_c \rangle = f_3 \langle \delta^2 T \rangle / \langle T \rangle^2 \quad (11)$$

(where $\langle \rangle$ = time-averaged quantity; ϵ_c, ϵ_L = continuum, line emission coefficients; $\epsilon_{c_0}, \epsilon_{L_0}$ = continuum, line emission coefficients in the absence of fluctuations; $\delta^2 \epsilon_c$ = mean-square fluctuation of continuum emission coefficient; T = temperature; $\delta^2 T$ = mean-square fluctuation of temperature.) In Fig. 7 are shown the time-averaged radial distributions of temperature and of rms fluctuations for a low speed (subsonic) turbulent DC arc.

Nonequilibrium effects may play an important role in cases involving circuit interruption devices (in the thermal and dielectric recovery regimes), in strongly accelerating (as in converging-diverging nozzles) and decelerating flows (through shock waves) and within jets and confined columns. Spectroscopic methods, in conjunction with analytical formulations (16,17), have been applied to determine requisite temperatures and particle densities. The equations employed are those for the line emission coefficient, continuum emission coefficient, Saha equations, equation of state, and Boltzmann factors. The relation between the

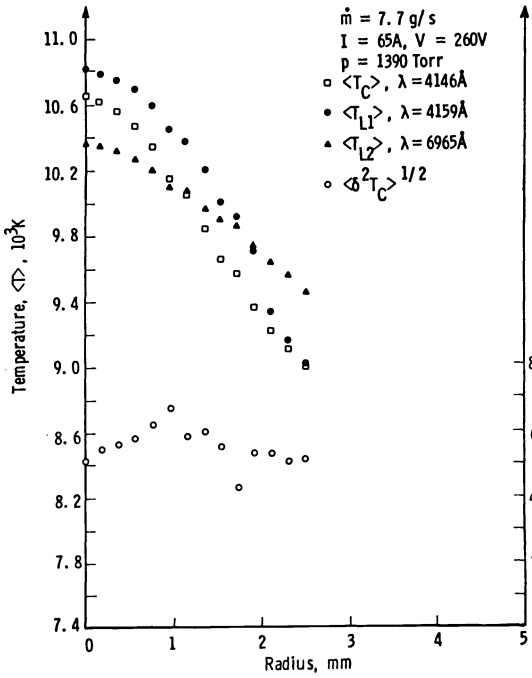


Fig. 7. Time-averaged radial distributions of temperature and of rms fluctuations for a turbulent DC argon plasma; $\dot{m} = 7.7 \text{ g/s}$, $I = 65 \text{ A}$ (Ref. 14).

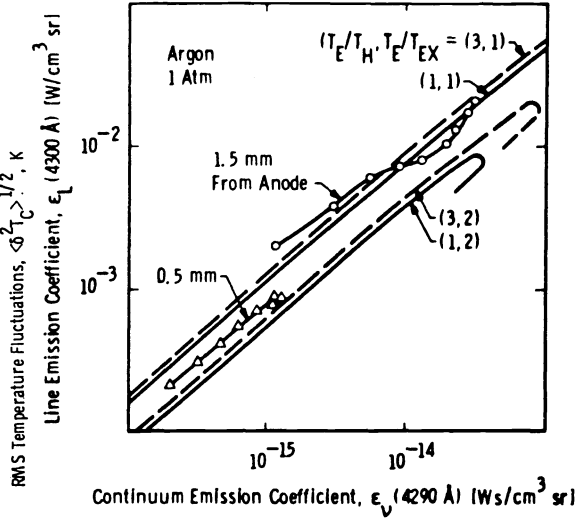


Fig. 8. Plasma characteristics based upon line and continuum coefficients (Ref. 16).

line and continuum emission coefficients is expressible in terms of T_{ex} , T_e/T_h , T_e/T_{ex} (where T_e = electron temperature, T_{ex} = excitation temperature of ions and atoms, T_h = temperature of heavy particles):

$$\epsilon_L = \frac{hc}{4\pi\lambda} A_{mn} n_m \quad (12)$$

$$\epsilon_c = \frac{16\pi e^6}{3c^3 (6\pi m_e k)^{1/2}} \frac{n_e^2}{T_e^{1/2}} \xi(\nu, T_e, T_{ex}) \quad (13)$$

$$\frac{n_e n_i}{n_a} = \frac{2Z_i (T_{ex,i})}{Z_a (T_{ex,a})} \frac{(2\pi m_e k T_e)^{3/2}}{h^3} \exp \left[-\frac{E_{\infty}}{k T_{ex,a}} \right] \quad (14)$$

$$p = (n_a + n_i) k T_h + n_e k T_e \quad (15)$$

$$\frac{n_o}{g_o} = \frac{n_{\infty}}{g_{\infty}} \exp \left[\frac{E_{\infty}}{k T_{ex,a}} \right] \quad (16)$$

$$\frac{n_m}{g_m} = \frac{n_n}{g_n} \exp \left[-\frac{E_m - E_n}{k T_{d_{\infty}}} \right] \quad m, n > m^* \quad (17)$$

$$\frac{n_e n_i}{n_m} = \frac{2Z_i (T_{ex,i})}{g_m} \frac{(2\pi m_e k T_e)^{3/2}}{h^3} \exp \left[-\frac{E_{\infty} - E_m}{k T_{d_{\infty}}} \right] \quad (18)$$

(where A_{mn} = transition probability; c = speed of light; e = electron charge; E_m, E_n = energy at level m, n ; E_{∞} = ionization energy; g_m, g_n, g_o = statistical weight of level m, n ground state; h = Planck's constant; k = Boltzmann constant; m_e = electron mass; n_a, n_e, n_i = number density of atoms, electrons, ions; n_m, n_n, n_o = population density of level m, n , ground state; p = pressure; $T_{d_{\infty}}, T_e, T_{ex,a}, T_{ex,i}, T_h$ = upper level distribution temperature, electron temperature, excitation temperature of atoms, excitation temperature of ions, heavy particle temperature; Z_a, Z_i = internal partition function of atoms, ions; ϵ_L, ϵ_c = line, continuum emission coefficient; ν = frequency; ξ = correction factor.)

Further, it is assumed that

$$T_{ex,a} = T_{ex,i} \text{ and } n_e = n_i \quad (19)$$

Results of the calculations of line and continuum emission coefficients, as functions of T_e/T_h and T_e/T_{ex} , are given in Fig. 8. Experimental measurements of the line and continuum emission coefficients (at various radii) are also shown in Fig. 8, indicating the presence of nonequilibrium at various radial locations within the column. As can also be observed, one disadvantage of this method rests with the relative insensitivity to large changes in the parameters - or, alternatively, the method exhibits a strong sensitivity to experimental errors.

LASER-INDUCED FLUORESCENCE

Laser-induced fluorescence (LIF) in atoms was conceived as a method of trace analysis soon after the invention of the dye laser in 1966 (18). It was speculated that as little as a single atom could be detected using the method of laser induced resonant fluorescence (19). Experimentally, concentrations of sodium as low as 10^{10}cm^{-3} were detected in 1971 using this method (20).

Soon afterwards, the real potential of LIF, as applied to molecules, was recognized by chemical kineticists. In this case, energy state population distributions of short-lived chemical species during chemical reactions could be measured and state-to-state chemical reactions studied for the first time. Since the pioneering work of Zare and Dagdigian, (21) the technique of LIF has become recognized as a well-established laboratory method for chemical dynamics studies. LIF has been applied to study the products of basic model type reactions (22), multi-photon dissociations (23), as well as more complicated situations such as surface catalysis (24). Information on state populations, kinetics of energy transfer, and lifetime of various species can be obtained.

The LIF method advanced from a laboratory scientific investigative tool to an applied analytical tool when it was employed in the study of combustion processes (25). In this "real life" application, both the sensitivity and the ability to give internal energy state distributions were recognized and exploited. The sensitivity is necessary in order to study the true radicals, particularly the hydroxyl group, which, although present only in small quantities, can affect greatly the kinetics and dynamics of the combustion process. Moreover, the ability to measure the internal energy distributions provides a measure of the rotational-vibrational temperature of these species. As explained in the following, the LIF method has good spatial and potential for temporal resolution and, thus, can provide very important experimental data on the integral dynamics of the flame.

Despite the similarities with combustion studies, however, the LIF method has not yet been applied to investigate plasma chemical processing and plasma arc devices. It is believed that conditions and requirements for the diagnostics of plasma devices are quite similar to the study of combustion processes: moderately high temperatures (in the range of several thousand degrees Celsius), (possible) nonequilibrium gas composition, multitude of transient species, and the need for a probe that does not (significantly) perturb the dynamics of the system. It is anticipated that the application of LIF could fill an important gap in the diagnostics of plasma devices and processes and also provide some basic, important data on their optimization.

LIF mechanisms

When an atom or molecule is excited by a laser to an excited state, the excitation may decay back to the ground via different mechanisms. The decay can be radiative (emitting photons), or non-radiative, or may even be dissociative. Figures 9 and 10 show the different relaxation mechanisms for the case of atoms and molecules, respectively. The molecular case is considerably more complicated due to the added degrees of freedom.

Processes (a) and (b) in Figs. 9 and 10 are considered as laser-induced fluorescence mechanisms. The other processes represent loss channels. The fluorescence quantum efficiency is defined as the average number of fluorescent photons per unit photon absorbed - and is always less than unity. Generally, atoms have higher photon yield than molecules; diatomics tend to have higher quantum efficiencies than larger molecules.

The intensity of fluorescence is given by the spontaneous emission rate in the excited non-equilibrium system. The spontaneous emission intensity for an atom is given by

$$I = \hbar\omega_{21} N_2 A_{21} \quad (20)$$

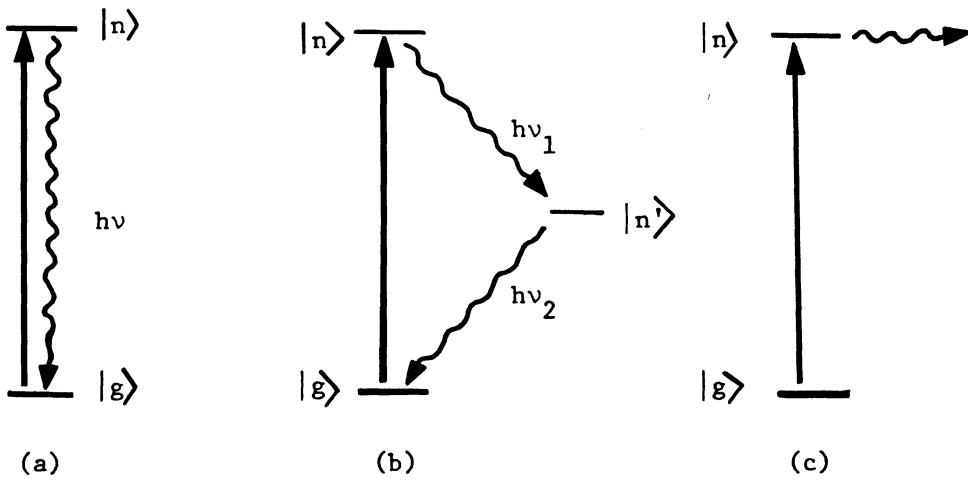


Fig. 9. Possible laser induced processes in an atom: (a) resonant fluorescence, (b) fluorescence via an intermediate state, (c) collisional energy transfer.

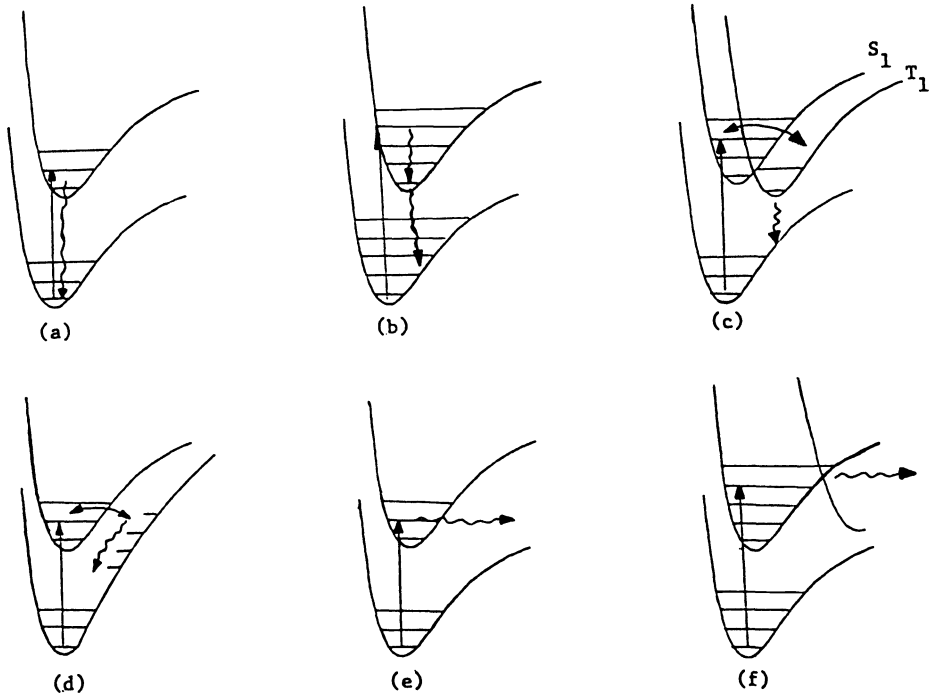


Fig. 10. Possible laser induced processes in a molecule: (a) resonant fluorescence, (b) indirect fluorescence, (c) phosphorescence, (d) non-radiative decay, (e) collisional energy transfer to a quencher, (f) predissociation.

(where A_{21} = transition probability, $h = h/2\pi$, h = Planck's constant, N_2 = population density of the excited state, ω_{21} = frequency of the transition.) Since each atom can be excited many times and therefore emit radiation many times, resonant fluorescence can be a very sensitive method of detecting an atom. For example, at a low laser intensity of 21mW/cm^2 , there will be $\sim 2 \times 10^7$ scattered photons from a single sodium atom per second. The ultimate limit to the sensitivity comes from blackbody radiation, scattering of the incident laser by walls and particulate matter, and elastic scattering by molecules and atoms. In resonant fluorescence measurements, the rejection ratio of the incident laser becomes the dominant sensitivity limiting factor. With careful alignment and baffling, a rejection of 10^{-10} should be obtainable.

In Eqn. (20), only the total fluorescence yield is given. There is definitely a frequency spread due to the lineshape of the emission. The details of the lineshape of a resonant fluorescence process have been the subject of many studies (26). The subject is of important theoretical interest and can yield important basic quantum physics about two level systems. There certainly exists a relationship between the linewidth and the LTE temperature of the plasma. Due to the narrowness of the resonant fluorescence lines and to the multitude of competing processes (such as collisional effects), however, the probability of obtaining temperature information from atomic resonant fluorescence spectral broadening is small.

As discussed by Bradshaw et al (27), however, temperatures can be deduced from atomic fluorescence if certain conditions are satisfied. In these methods, atomic additives with low-lying excited states (e.g., In, Tl, Pb, Ga) are added to the flame. In a brute force manner, the ratio of the populations in the ground state and the first excited state is obtained by exciting the mixture at different frequencies. Specifically, in one of the schemes (Fig. 11), the fluorescence from level 3 to 1, when the atom is excited from level 2 to 3, is given by

$$B_{F_{3 \rightarrow 1}} = \frac{\ell}{4\pi} A_{31} h\nu_{31} n_3 \quad (21)$$

2→3

(where ℓ = fluorescence length, ν_{31} = frequency spacing between levels 1 and 3, and n_3 = population density in level 3.) Similarly, the fluorescence from level 3 to 2, when the atom is excited from level 1 to 3, is obtained

$$B_{F_{3 \rightarrow 2}} = \frac{\ell}{4\pi} A_{32} h\nu_{32} n_3 \quad (22)$$

1→3

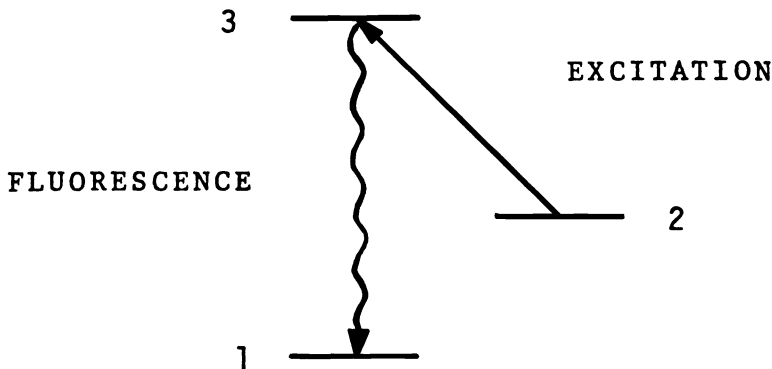


Fig. 11. Energy level diagram for atomic temperature measurement.

The population n_3 is different in both cases, however, and is related to n_1 and n_2 at equilibrium. Hence, the equilibrium population of n_1 and n_2 can be obtained. Assuming a Boltzmann distribution, this two line method yields a temperature, as shown in Eqn. (23). Provided saturation does not occur and the temperature is low enough so that the population in the upper excited state can be ignored, this method affords a continuous measurement of the temperature. As we shall see, this also implies a temporal resolution of the temperature.

$$T = \frac{h\nu_{12}/kT}{\ln\left(\frac{E_{\nu_{23}}}{E_{\nu_{13}}}\right) + 4 \ln\left(\frac{\nu_{13}}{\nu_{23}}\right) + \ln\left(\frac{B_{F_{3\rightarrow 2}}}{B_{F_{3\rightarrow 1}}}\right)} \quad (23)$$

(where $E_{\nu_{23}}$, $E_{\nu_{13}}$ = laser spectral intensities at frequencies ν_{23} and ν_{13}).

The fluorescence spectra from molecules are no longer simple lines but are complicated by rotational and vibrational fine structure. These complications are a blessing in disguise in that they provide a ready means of obtaining internal energy distribution and, hence, temperature information. The rate of fluorescence from a molecule is given by (25)

$$I = \sum_J, J'' h\nu_{J', J''} N_{J', A_{J', J''}} \quad (24)$$

(where $()'' = ()$ in the ground electronic state, $()' = ()$ in the excited electronic state, $J =$ rotational quantum number.) Equation (24) is simply an extension of Eqn. (20), where the excited state is now composed of many rotational lines. The energy level scheme is depicted in Fig. 10.

One important observation from Fig. 10 is that the fluorescence radiation frequency is generally different from the incident laser frequency. This implies that interference filters and other similar schemes can be used to discriminate against scattering of the incident excitation laser, which usually is the dominant sensitivity limitation to LIF. The sensitivity of LIF in molecules is, therefore, much enhanced.

Notice also that the right hand side of Eqn. (24) is summed over the excited states and is a function of the index J'' , the ground state rotational quantum number. Therefore, the integral fluorescence is a function of the ground state population. By tuning the laser frequency, one can obtain the vibration-rotational population distribution in the ground electronic state, provided all the rotational line strengths are known. From the internal population distributions, one can extract temperature data, assuming a Boltzmann type distribution function. Such distribution functions should be true in a plasma arc device which is collision dominated.

The sensitivity of the LIF method as applied to the detection of a particular chemical species arises from the ability to detect photons at very low signal levels. Photon counting techniques can easily provide sensitivities of a few counts per second even though normally, in LIF, the signals are much higher. According to estimates by Daily (28), the LIF method has a detectability limit of $\sim 10^4 \text{ cm}^{-3}$, with reasonable integration times and error limits. This number can be reduced if accuracy would be sacrificed and integration would be carried out for longer times. With respect to the detection of a molecule in a very dilute mixture, a sensitivity of 1 part in 10^9 can be obtained.

In addition to the sensitivity and ability to extract temperature information, LIF can also provide selectivity and spatial and (potentially) temporal resolution. The selectivity is inherent in the spectroscopic nature of this detection scheme. Individual molecular species concentration and temperature can be obtained in a mixture of different components. The spatial and temporal resolution is due to the coherent properties of the laser. One can focus the laser into specific regions of the plasma under study and obtain spatial variations of concentrations and temperature. Ultimately, the resolution is limited by the wavelength of the laser used, which is submicron. In practice, one is limited to larger spatial volumes due to optical aberrations and the desire to illuminate many molecules. Typically, a spatial resolution of 0.1mm can be obtained.

The temporal change in the temperature and concentration of the chemical species desired could be obtained if a cw laser is used. The ultimate resolution becomes a trade-off between signal strength and integration time. The lower limit is determined by the fluorescence time of the molecules, which is typically of the order of 10^{-8} s. A specific example of the detection of the SF radical in a SF₆ plasma arc current interrupter will be provided in the following section.

The temperature range of the atom or molecule to be measured by the LIF method is extremely wide. In principle, there is no high temperature limit. All that is required is the presence of a desired concentration of the species under study. At the low temperature end, the limitations are quite different with respect to atoms and molecules. For the case of atoms, the lowest excited state must be populated; for molecules, the lowest rotational states must be populated. Thus, for atoms, the lower band for temperature may be $\sim 2000\text{K}$ while for molecules, it may be as low as 20K. These lower temperature limits are considerably

lower than is found with emission spectroscopy methods where (for some gases) the lower temperature limits are $\sim 4000\text{K}$ (8).

Comparison with conventional plasma diagnostic methods

The advantages of LIF include (1) nearly non-intrusive, (2) high sensitivity as compared to typical spectroscopic measurements, (3) a wide temperature range, (4) certain components can be selectively detected out of a complicated mixture, (5) high spatial resolution, and (6) potential for temporal information.

LIF is not without its drawbacks, however. The most obvious limitation is the availability of laser radiation to induce the fluorescence. It has been assumed that any molecule can be detected by LIF. This is true only if the right frequency laser is available. Most molecules fluoresce in the UV region of the spectrum, where good coherent sources are still being developed. For example, the hydrogen molecule has a first electronic transition at 91689cm^{-1} , or 1091 \AA , in the VuV where a coherent source is still under intensive development (29). This problem is rapidly being solved by the burgeoning advances of laser technology and non-linear optics. Various reliable frequency mixing and frequency multiplication schemes are being developed (30). XuV wavelengths as short as 51nm have been obtained by harmonic generation in atomic vapors. Frequency mixing in a resonant medium provides tunable XuV down to 120 nm . Commercially, reasonably tunable high power UV radiation is obtainable down to 212nm . Recent developments in excimer lasers, tunable excimers, and excimer pumped dye lasers provide convenient tunable UV radiation for LIF. The free electron laser is also emerging as a high power laser source that is continuously tunable from XuV to the far IR (31). At present most atoms and molecules of interest can be studied with LIF.

While the technological problem basically is solved, the scientific problem still exists: the availability of basic physical parameters, such as rotational line strengths, which are needed in order to interpret molecular LIF data. The solution to this problem is to rely upon theoretical and experimental studies to obtain the necessary data. Some compilations already exist in the literature and, in view of the growing application of LIF, this data base is bound to increase rapidly. Already, for the radical species of interest in combustion, extensive compilations have been prepared. The case of atomic fluorescence suffers less difficulties since atomic spectroscopic data are relatively abundant.

Finally, there is the factor of cost. LIF requires considerable instrumentation and capital investment; a typical experimental set up is shown in Fig. 12. Tunable lasers in the ultraviolet are, in general, quite expensive. In addition, a data acquisition system is required for obtaining spatial and temporal information. This initial cost, though not prohibitive, is a deterring factor in the application of LIF.

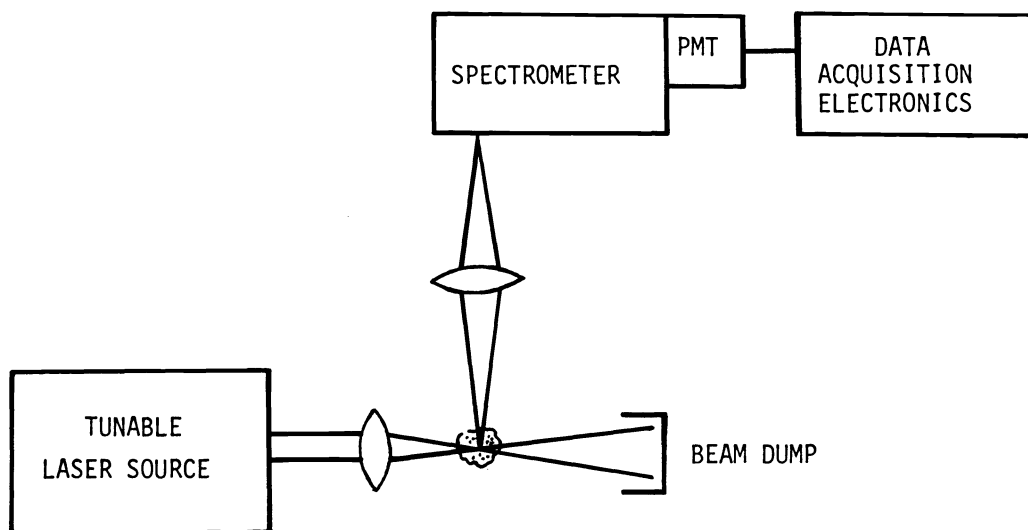


Fig. 12. Typical experimental set up for laser induced fluorescence measurements. (PMT = photomultiplier tube).

Specific cases of LIF

Consider first, LIF in OH. This is a classical case in combustion research. (On the other hand, the LIF of SF and BN are, here, conjectured examples of the application of LIF to plasma devices and processing.)

OH is probably the most studied radical in LIF because of its importance in combustion studies. Most of its spectroscopic data are available in the literature. LIF in OH can be used as a test for various combustion theories and models. Bechtel (32) showed that, in a premixed laminar flame, the OH radical temperature is the same as the N_2 temperature. He also showed that the population distribution in OH follows a Boltzmann law. These results were obtained by measuring the excitation spectrum of LIF in OH.

Recently, Chan and Daily (33), using a different approach, obtained the translation temperature of the OH radical in a flame. In their method, no assumption was made about the Boltzmann character of the excited state population distribution. If the functional forms of all the rotational and electronic relaxation rates are known, then the temperature can be obtained by regressively fitting the fluorescence spectrum under excitation conditions. This method has the merit that, if an optical multichannel analyzer is used, the temperature can basically be measured in a single shot. This capability is of great advantage in the cases of turbulent flames and turbulent arc devices.

Consider, now, the plausibility of using LIF in two plasma applications: (1) the measurement of particle concentration and temperature as a function of position and time in the recovery region of a plasma arc current interrupter and (2) the measurement of reactant temperature in a plasma torch chemical vapor deposition process.

The warm dielectric recovery period following arc interruption plays a critical role in determining the performance of a circuit breaker. Following thermal recovery (of the order of μs in SF_6), the heated column enters the warm dielectric regime - some hundreds of micro-seconds duration and with temperature in the range of 1000K (34). The exact recovery mechanisms and the role of turbulence has not been fully established. According to Kopainsky (24), the gas composition changes from a mixture of S, F, F^\pm , e^- to gradually increasing SF, S_2 and F_2 (and eventually to SF_6). LIF is particularly suited to monitoring the concentration of these atomic and diatomic species as a function of time, using a cw laser. At the same time, the history of the temperature can also be determined, providing an independent check on the calculated relationship between particle concentration and temperature (34).

The spectroscopic details of S_2 and F_2 are relatively well-known while those of SF are quite scarce (35). For S_2 , the $B^3\Sigma_u^- - X^3\Sigma_g^-$ transition at $31,835\text{cm}^{-1}$ can be used for LIF. The same spin multiplicity and symmetry guarantees a reasonable transition strength. Similarly, for F_2 , the $X^1\Sigma_g^+ - A^1\Pi_u$ transition can be employed. The frequency is in the range of $34,500\text{cm}^{-1}$. These two molecules can be excited with commercial Nd:Y laser pumped dye laser systems having output frequency doubling (34).

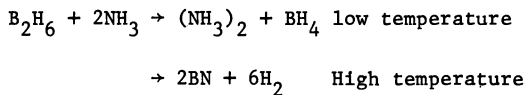
For SF, the laser requirement is less stringent. The first electronic band occurs at $25,000\text{cm}^{-1}$. The ground state is split by spin-orbit coupling into the $X_1^2\Pi_{3/2}, X_2^2\Pi_{1/2}$ states with a spacing of 401cm^{-1} (36). Likewise, the first excited state is split into $A_1^2\Pi_{3/2}$ and $A_2^2\Pi_{1/2}$. Ideally, the LIF signal should change as a function of time, indicating the formation of SF (cooling of S, F^\pm , F) and the disappearance of SF_6 (cooling of SF and formation of larger molecules).

In addition, the concentration of S, F, F^\pm can be measured using the method of atomic resonant fluorescence. The energy level schemes of these atoms are well established. Hence, the time history of all the species present in the recovery region of the SF_6 circuit breaker can be monitored. This complete characterization, especially in the temperature range from 3000K to 1,000K has not been achieved and should provide important design data for future circuit breakers.

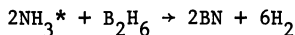
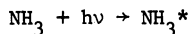
The potential success of the above schemes is supported by signal estimates. Using a 6W argon ion laser, one should be able to obtain lmW of tunable UV radiation at 4000 \AA , with a linewidth of 1cm^{-1} . Assuming a spatial resolution of 0.1mm , the laser intensity is, therefore, $\sim 10 \text{ W/cm}^2$ or $2 \times 10^{19} \text{ photon/sec/cm}^2$. Even with a moderate quantum efficiency, this photon intensity should produce at least $1.5 \times 10^3 \text{ photons/sec/sr}$ per atom or molecule using an integration time of 10nsec . A concentration of $>10^{10}\text{cm}^{-3}$ is expected for all important species in the SF_6 circuit breaker (34). Therefore, there is a sufficiency of photons from LIF to be detected. Basically, the instantaneous change in concentration of SF can be measured with this method.

Consider, next, some plasma chemical processes. One of the most important applications in the semiconductor industry is the reactive heating of the plasma in chemical vapor deposition. Thin films of BN have been obtained by the reaction of diborane and ammonia heated by a plasma (37). This large bandgap III-V compound semiconductor may have potential application in microwave devices. Moreover, cubic BN is one of the hardest ceramic materials known.

The reaction proceeds as



Since the internal energy of BN must be an important parameter in determining the crystallization process, it becomes important to be able to measure and possibly control its temperature after the chemical reaction. One method is to excite the reaction via laser excitation, in place of conventional plasma heating (38). The tunable output of a high power CO_2 laser can excite ammonia selectively and increase its reactivity. Thus



It is hoped that the state of the BN produced in the second reaction can be controlled by varying the NH_3 excitation.

Regardless of which method is used to produce BN, its temperature has to be determined non-intrusively. This is where LIF could be used effectively. One could measure the BN temperature by exciting the $X^3\Pi \rightarrow A^3\Pi$ band at $27,877\text{cm}^{-1}$. This can be separated at various reaction conditions by changing the plasma heating or CO_2 laser intensity.

INTERFEROMETRY

The interference process (39) arises from the combination of two light waves of the same wavelength, and of a constant difference in phase, to produce a wave with displacement equal to the sum of the displacements of the individual waves. Interference occurs when

$$n_1 \ell_1 - n_2 \ell_2 = N\lambda \quad (25)$$

(where ℓ_1, ℓ_2 = optical path length in medium 1,2; n_1, n_2 = index of refraction of medium 1,2; $N = 0, 1, 2$ (bright fringes); λ = wavelength of source.) The resulting fringe patterns contain dark bands (through the cancellation of two light waves of equal intensity and opposite phase) and light bands (from the addition of waves having zero phase difference). Two-beam interferometers (such as the Mach-Zender, Fig. 13) provide two separate paths for the light between the source and the point (the detector) at which the two beams are recombined. One beam, the test beam (i.e., the object wave or the comparison wave), passes through the section of interest (e.g., the plasma). Simultaneously, the second beam, the reference beam (from the same source), passes outside the test section. The deflection produced at a given point in the fringe pattern is proportional to the change in optical path length introduced by the part of the test object that corresponds to the given point. The

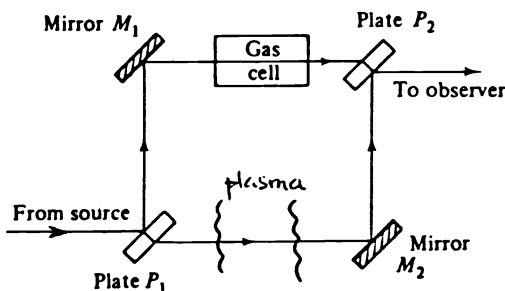


Fig. 13. Mach-Zender interferometric arrangement.

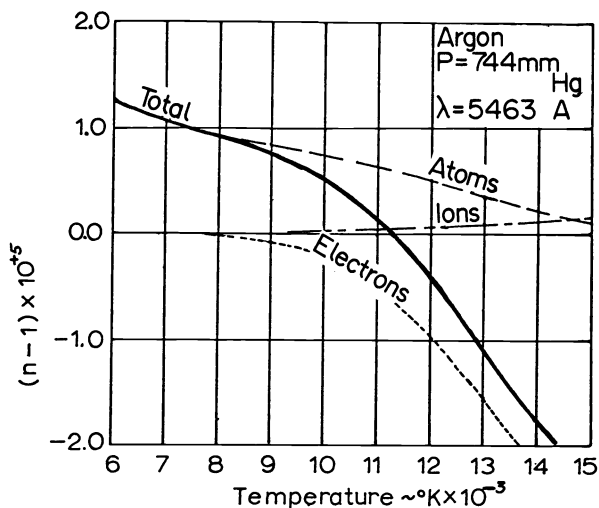


Fig. 14. Refractivity of argon as a function of temperature (Ref. 39).

fringe shifts in this case correspond to the values of index of refraction. In differential interferometry, the reference beam is not used. The fringe pattern formed in the image plane is associated with the difference in the change of optical path of two beams that pass through the test section at slightly different heights (40) (with consequently differing optical paths); here, the fringe shifts correspond to gradients in the index of refraction.

The phase shift of light through a phase object (say, the plasma) is associated with the local index of refraction, n , which, in turn, can be expressed in terms of the dispersion relation, leading to

$$n-1 = (n-1)_{\text{atoms}} + (n-1)_{\text{electrons}} + (n-1)_{\text{ions}} \quad (26)$$

$$= \sum_i K_i N_i \quad (27)$$

(where K_i = specific refractivity of i th component (atoms, ions, electrons), N_i = number density of i th component.) The temperature dependence of the index refraction is illustrated in Fig. 14, for atmospheric argon. For regions where dissociation is negligible, the Gladstone-Dale relation may be used

$$n-1 = K \rho \quad (28)$$

(where K = Gladstone-Dale constant for the medium, ρ = gas density.)

With the Mach-Zender arrangement (Fig. 13), as noted earlier, the object wave and the reference wave traverse different physical regions. This method then suffers a principal disadvantage in requiring precision optical components and precision alignment. These disadvantages are overcome using holographic interferometric techniques such as double exposure (3,41) or real-time (41) techniques. Both methods involve two steps: (1) the formation of a hologram under reference conditions, using a comparison wave through the test section and, later, (2) the passage of a second wave, the object wave, through the test section at operating conditions. The ultimate interference patterns then involve the object wave and the comparison wave. Since these waves have traversed the same geometric field, precision optical components are no longer needed. In effect, these methods can be classified as single path interferometry. A disadvantage results, associated with the need (and the setup time) for a second operation. A holographic interferometry arrangement is shown in Fig. 15.

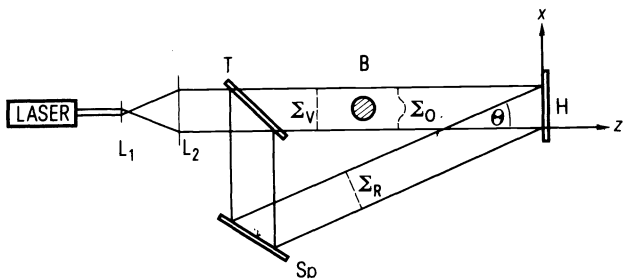


Fig. 15. Holographic interferometry arrangement for the observation of transparent objects. B = arc (phase object); H = holographic plate; L_1, L_2 = lens system; S_D = mirror; x, z = coordinates; θ = angle; $\Sigma_V, \Sigma_O, \Sigma_R$ = comparison, object, reference waves (Ref. 41).

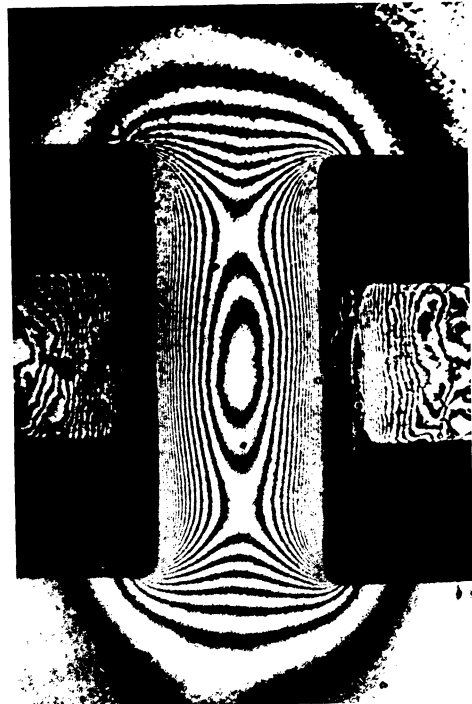


Fig. 16. Interferogram obtained with double exposure method. Cold gas flow through the cylindrical gap in a dual flow nozzle system (Ref. 41).

precision optical components are no longer needed. In effect, these methods can be classified as single path interferometry. A disadvantage results, associated with the need (and the setup time) for a second operation. A holographic interferometry arrangement is shown in Fig. 15.

In double exposure holographic interferometry (41) the first hologram is recorded under base or reference conditions (e.g., with cold flow (absence of plasma)), recording essentially the undistorted comparison wave, Σ_V ; the reference wave, Σ_R , is also directed to the holographic plate. A short time later (typically) a second hologram is imposed upon the undeveloped plate; here, now the plasma is present and the instantaneous state of the object wave, Σ_O , during the second exposure, is stored. The holographic plate is now developed and is then illuminated by the reference wave, Σ_R . Both Σ_V and Σ_O are thereby reconstructed. Since these waves are coherent, they interfere in the same way as would the two waves emerging from a conventional Mach-Zender interferometer. Figure 16 illustrates an interferogram obtained with cold gas flow in a dual flow system.

Another example of holographic interferometry is illustrated in Fig. 17 (42). The upper portion of the figure shows the different spatial regions covered by emission spectroscopy and by interferometry - illustrating the complementary nature of these methods. The lower portion of Fig. 17 presents the radial distribution of temperature as determined from the measured fringe shifts, the inversion of these data, and the (known) refractivity of air. (In many cases, e.g., nitrogen and sulfur hexafluoride, a range of temperature (more or less substantial) will be found in which the refractivity will be relatively insensitive to temperature; in this region, then, temperatures determined according to the refractivity will tend to be less accurate compared to those outside the range noted and to those found from spectroscopic techniques.)

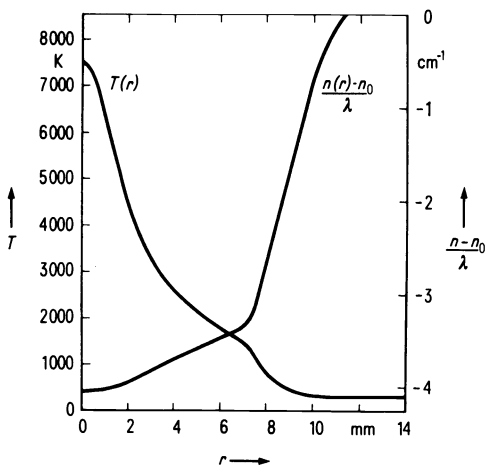
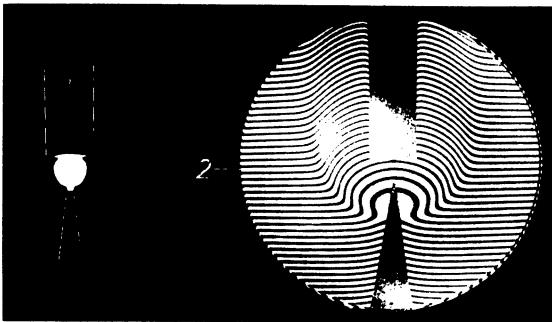


Fig. 17. Free burning, 6A atmospheric air arc. Upper: self light and related interferogram. Lower: radial distribution of index of refraction and temperature (Ref. 42).

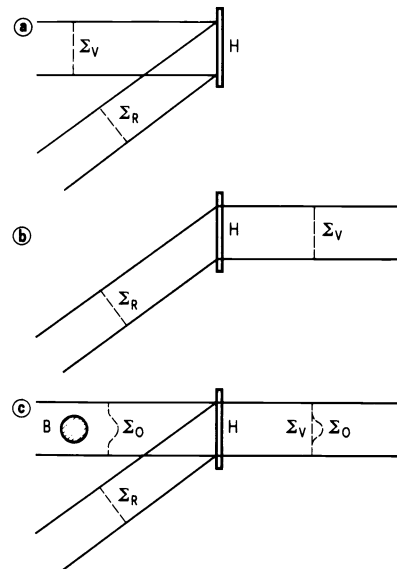


Fig. 18. Principle of the real-time holographic interference method. (a) Storage of the comparison wave Σ_V , (b) Reconstruction of the comparison wave Σ_V , (c) Interference of the object wave, Σ_O , and the reconstructed comparison wave (Ref. 41).

Real-time holographic interferometry enables the recording of a sequence of interferograms (in contrast to the single recording which can be obtained using the double exposure method) - a particularly useful technique in the case of a time-varying phase object (e.g., a plasma). The procedure (41) is illustrated in Fig. 18. The first step is that described earlier - obtaining a hologram under base or reference conditions (employing Σ_V and Σ_R). The plate is then developed (preferably in-situ). Illumination of the plate by Σ_R reconstructs Σ_V (part (b) of Fig. 18). The phase object (the arc) is energized and the object wave, Σ_O , is passed through the test section (part (c) of Fig. 18). The time varying object wave passes through the transparent hologram and is superimposed upon the previously reconstructed, coherent comparison wave. The resulting interference phenomena change continuously with changes in the plasma; the phenomena can be recorded by a high speed camera. A continuous wave laser is required for the light source.

Differential interferometry (39,40) using the Wollaston prism, is yet a simpler approach, requiring but a single exposure to obtain an interferogram. The method is sensitive to gradients in the index of refraction, in contrast to the techniques described previously. The index of refraction can be found through appropriate integration.

As noted in Ref. 40, the Wollaston prism contains two prisms of crystalline quartz, whose optical axes are perpendicular both to one another and to the direction of the incoming beam (Fig. 19). With incoming light linearly polarized at 45° to the axis of the crystal, the beam will be split into two equal components (ordinary and extraordinary rays) in the first half; these travel at different speeds and are orthogonally polarized. Due to the orientation of the second half, the ordinary and extraordinary rays of the first prism half become the extraordinary and ordinary waves, respectively, in the second half. Since the two beams see a difference in the index of refraction at the dividing plane, they emerge from the prism with a small angular separation, ϵ . The two beams leaving the prism have a phase difference that is proportional to their distance, h , from the mid-plane; this effect can be used to produce equally spaced interference fringes parallel to the apertures of the prisms. With the outgoing beams orthogonally polarized, a 45° polarizer placed behind the Wollaston is used to obtain components that can interfere.

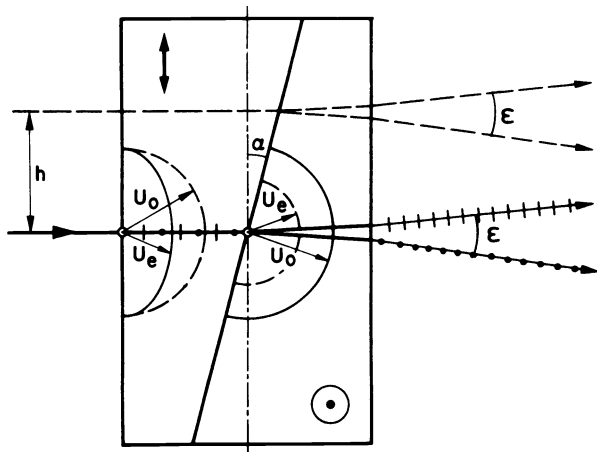


Fig. 19. Rays in a Wollaston prism. Separation of the wavefronts is indicated by u_o and u_e (Ref. 40).

An optical arrangement is shown in Fig. 20. The image point P_1', P_2' corresponds to two points P_1 and P_2 in the object plane separated by a distance, Δy . Thus, as noted earlier, the differential interferometer measures the difference in the change of optical path of two test beams that pass the object at slightly different values of y - measuring, then, the gradient, $\Delta n/\Delta y$. By rotating the Wollaston prism, the polarizer, and the plane of rotation of the incoming beam, the orientation of the fringes will similarly change. The technique leads to the determination of density gradients normal to the undisturbed fringe pattern.

In Fig. 21 are shown fringe patterns for a high current plasma, with the fringe patterns at different orientations (horizontal, 45° , vertical), indicating sensitivity to gradients in the vertical ("radial"), both vertical and axial, and axial directions, respectively. The last named pattern indicates the presence of but relatively small gradients in the axial direction. The second orientation permits determination of the size of the core and of the adjacent thermal boundary layer. The first noted orientation provides, in principle, the

basis for determining the radial distribution of temperature.

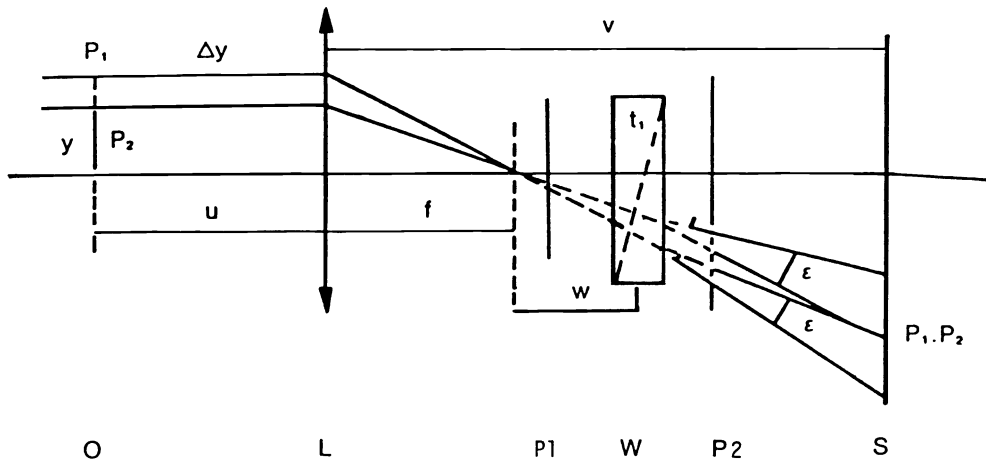


Fig. 20. Optical arrangement for differential interferometry (L = objective lens, O = object plane, P1, P2 = polarizer 1, 2, S = screen (image plane), W = Wollaston prism) (Ref. 40).

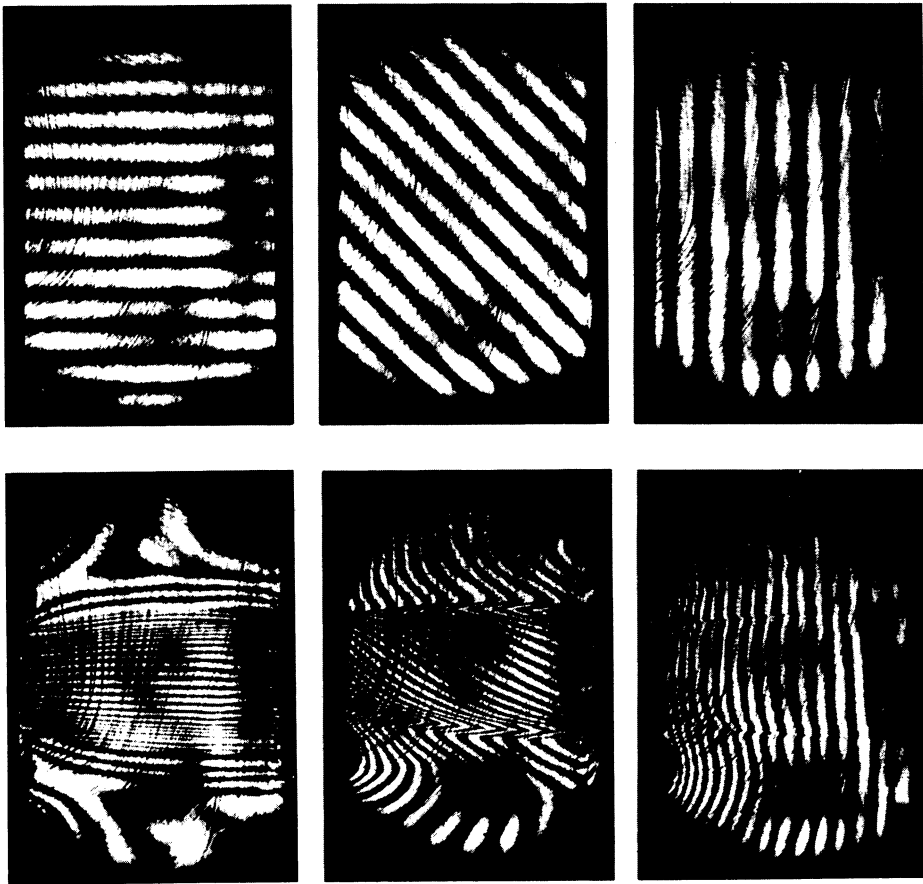


Fig. 21. Fringe patterns obtained with a high current arc using a differential interferometer with different fringe orientations (upper row - undisturbed fringes) (Ref. 40).

Interferometry, as with spectroscopy, observes the phenomena along a line of sight. Consequently, it is necessary to invert (43) the measured fringe shifts (integrated along the path of interest) so as to obtain local values of the index of refraction and of temperature. Further, it should be noted that, owing to the use of a laser, interferometry becomes a nearly - although not totally - non invasive technique.

Interferometric methods are applicable in the absence of turbulence. The effects of turbulence, with the associated eddies and varying indexes of refraction, lead to a destruction of the fringe patterns.

LASER VELOCIMETRY

Laser velocimetry, although a moderately invasive technique, is one of the more powerful approaches employed to measure local velocity (in principle, all components) and its variance. The method makes use of the coherence properties of the laser to form a precisely definable grid in space (Fig. 22). An optical arrangement to accomplish this objective is

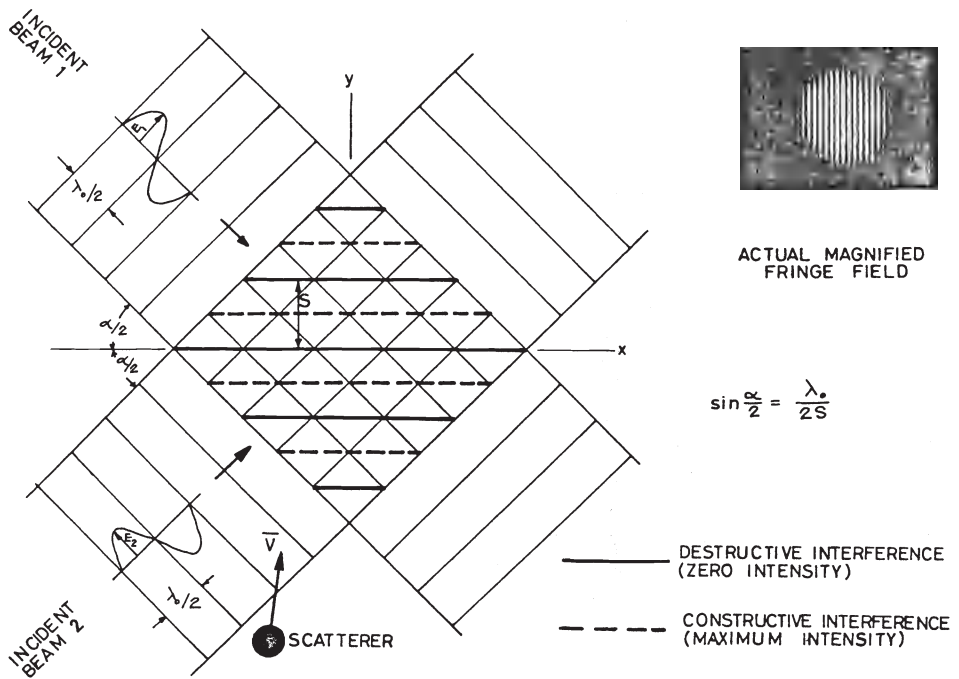


Fig. 22. Fringe pattern formed by two coherent crossed beams (Ref. 44).

shown in Fig. 23 (a forward scattering set-up). The (continuous wave) laser beam is split into two beams which are brought to a focus in the test section. The region of beam overlap (or the cross-over region or the probe volume) thus formed, as well as the fringe spacing, is determined by the geometry, optics, and the characteristics of the laser beam. The fringe spacing is given by

$$s = \frac{\lambda}{2 \sin \frac{\alpha}{2}} \tag{29}$$

(where α = beam convergence angle, λ = laser wavelength). The cross-over region is a distorted ellipsoid of revolution (44) having width, d , and length, ℓ , expressed as

$$d = \frac{d_0}{\cos \frac{\alpha}{2}} \tag{30}$$

$$\ell = \frac{d_0}{\sin \frac{\alpha}{2}} \tag{31}$$

$$\text{with } d_o = 1.184 \frac{\lambda f}{D} \quad (32)$$

(where D = laser beam diameter at lens face (as in Fig. 23), f = focal length of lens).

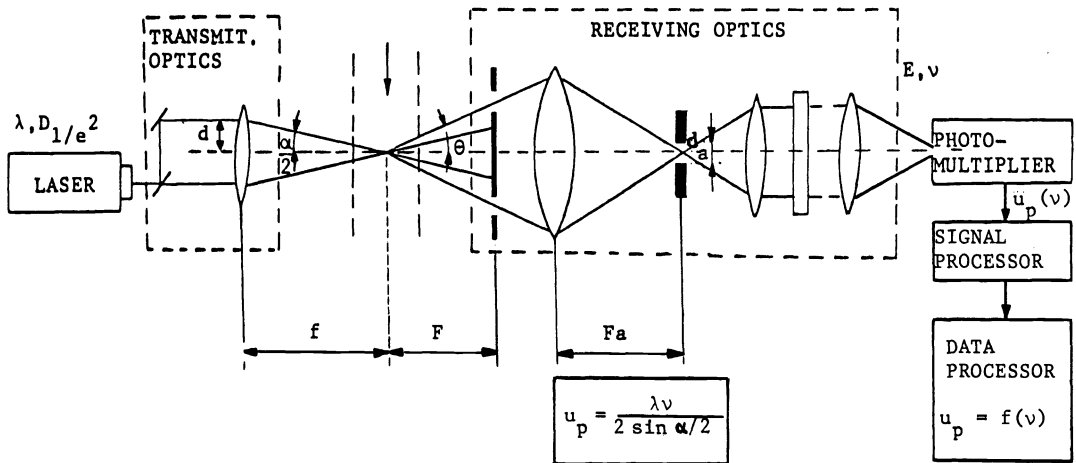


Fig. 23. Optical arrangement (forward scattering) for laser velocimetry (Ref. 45).

To determine velocity within the probe volume, scattering centers are introduced into the flowing medium; some of these particles penetrate this volume. Consider the component of velocity (or direction of motion) perpendicular to the fringes. During the traversal of the probe volume by a scattering center, light is scattered at each crossing of a bright fringe - leading to a traversal frequency, ν . The velocity (that is, the component normal to the orientation of the fringes) becomes

$$U_p = s\nu \quad (33)$$

A more fundamental approach (46), from the point of view of the Doppler shift in frequency of the scattered light from two coherent beams, yields the same result.

The scattering centers may be introduced (1) intentionally, as detectors to determine the flow field. Here, the particles tend to be relatively uniform in size and shape and reasonably able to follow the flow. To minimize their influence upon a plasma, the mass concentration should be relatively small; (2) intentionally, as an integral part of a plasma process. For this case, the particles may not be uniform, may not accurately track the flow, and may be in sufficient quantity so as to influence the plasma, and (3) randomly, as from electrodes or nozzle walls. These particles generally will not be uniform in size and shape, and will tend not to follow the flow; often, there will be relatively few such particles injected per unit time.

In using laser velocimetry to measure continuum flow velocities in a fluid (44), the scattering particles must be large enough to be out of the range of the free molecular range of the fluid and yet small enough to be able to follow accurately the motions of the fluid. These two limitations indicate that particle size should be of the order of $1\mu\text{m}$. Mie scattering of the light results for this case. The scattered intensity is a strong function of scattering angle, particle refractive index and size, and the polarization and intensity of the incident light. The scattering intensity for spherical particles is roughly proportional to the fourth power of the particle diameter and inversely proportional to the fourth power of the wavelength of the incident radiation. In Fig. 24 is shown Mie scattering from a $1\mu\text{m}$ sphere. Mie scattering is characterized by a strong forward scattering intensity, with substantial decrease in scattering intensity as the scattering angle increases. For the largest signal strength, the collecting optics should be placed in the forward scattering direction (as in Fig. 23).

Probe volume can be made sufficiently small for purposes of spatial resolution through a combination of beam convergence angle, α (the entrance optics), and the collecting optics (e.g., the annular aperture, lens, pinhole arrangement shown in Fig. 23). Ellipsoid dimensions, d and l , of 0.1mm and 0.7mm , respectively, have been achieved (45).

In many cases of practical interest, the flow field may be nonuniform, non-steady, perhaps turbulent, or may exhibit substantial acceleration (as in nozzle flow) or deceleration

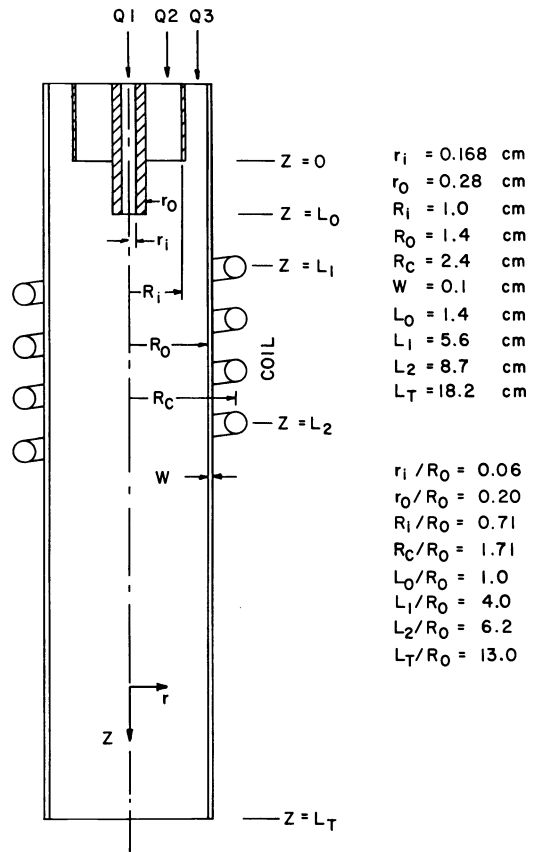
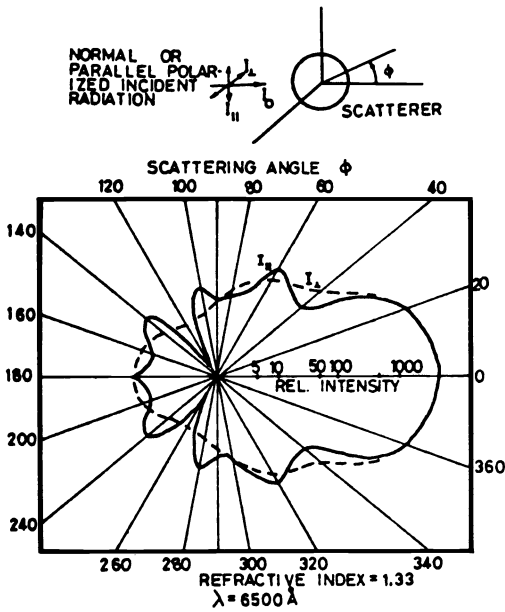


Fig. 24. Mie scattering from a $1\mu\text{m}$ diameter sphere (Ref. 44). Fig. 25. Plasma torch configuration (Ref. 47)

(through shock waves). Particularly in these instances, as well as within steady, uniform flow, the behavior of the particle may be such that neither its velocity nor its trajectory matches that of the flowing medium. The relation between the velocity and trajectory of the plasma and the scattering center becomes important to understanding applications involving plasma processing. Such relations for single particles have been obtained and have been applied to a variety of configurations (47,48). The axial (in the case considered, the configuration is oriented vertically) and radial momentum equations, respectively, are written

$$\frac{dU_p}{dt} = \left(\frac{-3}{4}\right) C_D (U_p - U_f) |U_R| (\rho_f / \rho_p d_p) + g \tag{34}$$

$$\frac{dv_p}{dt} = \left(\frac{-3}{4}\right) C_D (v_p - v_f) |U_R| (\rho_f / \rho_p d_p) \tag{35}$$

(where C_D = drag coefficient; d_p = diameter of the particle; g = gravity; t = time; U_f, U_p = axial velocity of the fluid, of the particle; U_r = relative axial velocity; v_p, v_f = radial velocity of the fluid, of the particle; ρ_f, ρ_p = density of the fluid, of the particle) with

$$C_D = C_D(R_e) \tag{36}$$

(where R_e = Reynolds number = $\rho_f U_f d_p / \mu_f$, and μ_f = viscosity of the fluid)

and

$$U_R = [(U_p - U_f)^2 + (v_p - v_f)^2]^{1/2} \tag{37}$$

The energy equation is expressed

$$mC_p \frac{dT_p}{dt} = hA(T_f - T_p) - A\sigma\epsilon (T_p^4 - T_a^4) \tag{38}$$

(where A = surface area of particle; C_p = specific heat; h = heat transfer coefficient; m = mass of particle; T_a, T_f, T_p = temperature of the surface of the particle, of the fluid, of the particle; ϵ = particle emissivity, σ = Stefan-Boltzmann constant.) The heat transfer coefficient is further expressed in terms of the Nusselt number, N_u (where $N_u = hd_p/k_{ave}$, and k_{ave} = average thermal conductivity.)

In accounting for melting, the temperature of the particle is assumed to remain constant once its temperature reaches the melting point, i.e., when $T_p = T_m$. The liquid fraction, x , of the particle is calculated through

$$\frac{dx}{dt} = \frac{Q_n}{m\lambda_m} \quad (39)$$

(where Q_n = net heat flux to the particle [the right hand side of Eqn. (38)], λ_m = latent heat of fusion.)

When the particle becomes completely molten (i.e., $x = 1$), its temperature is allowed to increase again until the boiling point, T_v , is reached. At this condition, the particle temperature remains constant, at T_v , while its diameter decreases due to evaporation, as shown by

$$\frac{d d_p}{dt} = \frac{-2 Q_n}{\pi \rho_p \lambda_v d_p} \quad (40)$$

(where λ_v = latent heat of vaporization.)

For the vertically oriented plasma torch configuration shown in Fig. 25, the streamlines and temperature contours are shown in Fig. 26. Trajectories, for $10\mu\text{m}$ and $250\mu\text{m}$ diameter particles, are shown in Figs. 27a and 27b, respectively. The essential differences in their paths are clearly evident, as is the portent to processing applications.

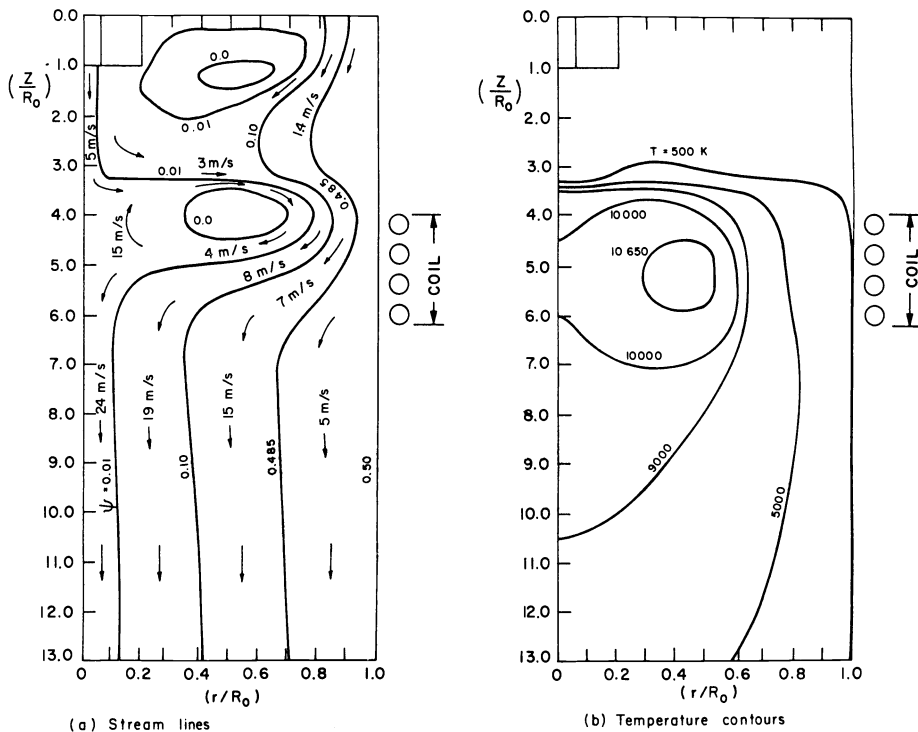


Fig. 26. Flow and temperature fields, $Q_1 = 0.4\text{ l/min}$, $Q_2 = 0.2\text{ l/min}$, $Q_3 = 16\text{ l/min}$ (Q_1, Q_2, Q_3 = particle carrier gas flow rate, plasma gas flow rate, sheath gas flow rate). (Ref. 47).

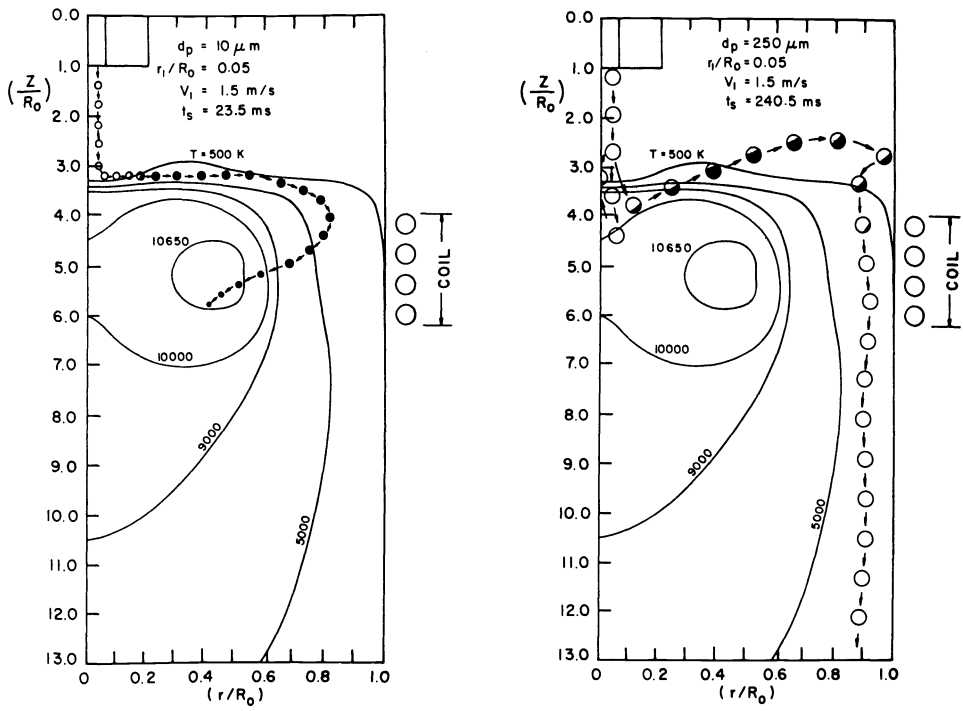


Fig. 27. Particle trajectories. (a) $d_p = 10 \mu\text{m}$, (b) $d_p = 250 \mu\text{m}$. (Ref. 47).

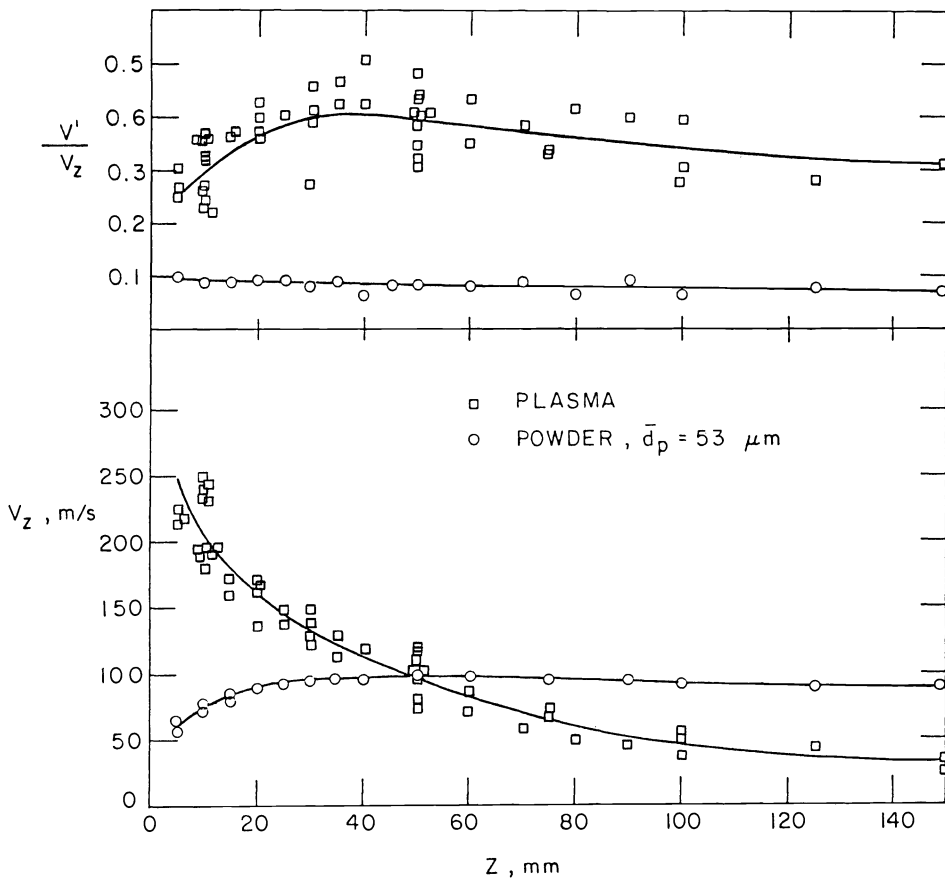


Fig. 28. Plasma and particle velocities and turbulence intensity along the outerline of a plasma torch (Ref. 48).

Measurements (48) of plasma and particle velocities and the turbulent intensity along the axis of a vertically oriented plasma jet are shown in Fig. 28. Here, the respective velocities were determined using particles of $1\mu\text{m}$ and $53\mu\text{m}$ diameter. The substantial inertia effects of the large particles is seen, both close to and distant from the jet entrance, in both the velocity and the turbulent intensity distributions.

The response of particles to turbulent flow fluctuations and to sudden deceleration (through a shock wave) is shown in Figs. 29 and 30, respectively. In both cases, significant degradation is found (reduced frequency response, long relaxation time) even with particles of but modest size, of the order of $1\mu\text{m}$ diameter. Such results point toward certain limitations in applying laser velocimetry methods to track flows that exhibit substantial acceleration or deceleration or that exhibit significant turbulence (in some plasma applications, turbulent frequencies are in excess of 1MHz). Assuming that the light scattering process can be expressed in terms of Mie scattering (44), decreases in size of the particles, so as to achieve improved tracking capability, will result in substantial reduction in signal (and in signal-to-noise ratio).

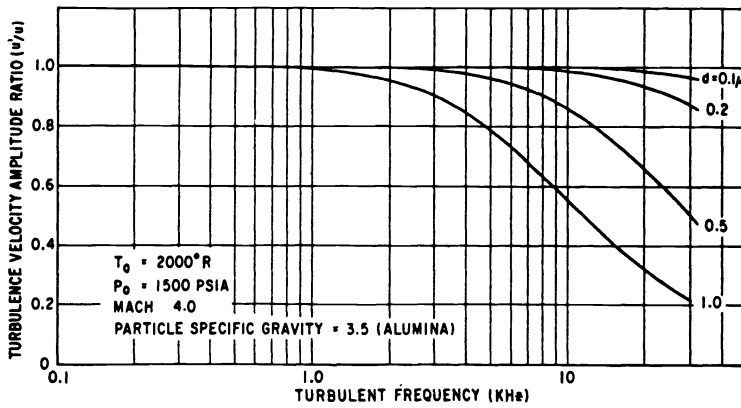


Fig. 29. Particle response to turbulent flow fluctuations (specific gravity of particle = 3.5 (alumina), Mach number = 4.0, $T_0 = 2,000\text{R}$, $P_0 = 1,500 \text{ psia}$). (Ref. 44).

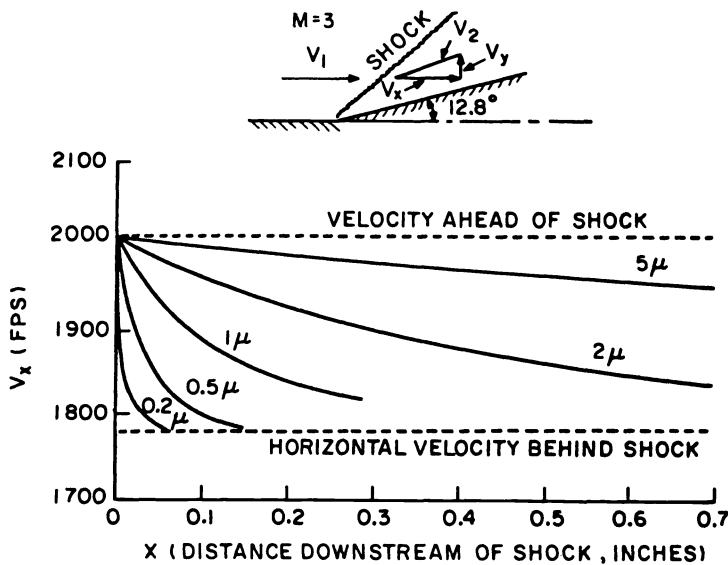


Fig. 30. Relaxation time associated with shock wave-particle interaction (Ref. 44).

SUMMARY

Four diagnostic methods applicable to the determination of temperature (and particle density) and velocity in plasmas have been reviewed: spectroscopy, laser induced fluorescence, interferometry, and laser velocimetry. Each technique has its advantages and limitations, indicating the need for measurements derived from a variety of approaches. Spectroscopy is non-intrusive, can provide good spatial and temporal resolution, and can be applied to turbulent flows, as well as to cases involving non equilibrium. Observation is along a line of sight, requiring inversion to obtain local values. Laser induced fluorescence is a nearly passive technique that can be applied over a wide range of temperature. Further, the method allows the selective measurement of one particular component of a mixture. Good spatial resolution can be obtained as well; there is potential for temporal resolution. Interferometric methods are also nearly passive. Through single path interferometry (double exposure, real-time, and differential), system requirements become much less restrictive than for classical Mach-Zender interferometry (a double path method). Good spatial and temporal resolution can be obtained. As with spectroscopy, observation is along a line of sight. Perhaps the most serious disadvantage of interferometry is the need to minimize the presence of turbulence. Laser velocimetry is a moderately invasive technique, a method of which permits adequate spatial resolution. Detailed information on the components of velocity and the variance can be obtained. The relation between measured particle velocity and that of the fluid medium can be complex, particularly when melting and evaporative processes occur.

REFERENCES

1. H.R. Griem, Plasma Spectroscopy, McGraw-Hill, New York, New York (1964).
2. T.L. Eddy, C.J. Cremers and H.S. Hsia, J. of Quant. Spect. and Rad. Trans. **17**, 287-296 (1977).
3. J. Thompson and M. Kristiansen, Eds., Plasma Diagnostic Seminar, Texas Tech University (1973).
4. C.D. Maldonado and H.N. Olsen, J. Opt. Soc. **56**, 1305-1313 (1966).
5. J.L. Wu and D.M. Benenson, IEEE Trans. on Pl. Sci. PS-5, 284-291 (1977).
6. Y. Yasutomo, K. Miyata, S.I. Himeno, T. Enoto and Y. Ozawa, IEEE Trans. on Pl. Sci. PS-9, 18-21 (1981).
7. P. Fauchais, K. Lapworth and J.M. Baronnet, Eds., First Report on Measurement of Temperature and Concentration of Excited Species in Optically Thin Plasmas, International Union of Pure and Applied Chemistry (1978).
8. A. Vardelle, J.M. Baronnet, M. Vardelle and P. Fauchais, IEEE Trans. on Pl. Sci. PS-8, 417-424 (1980).
9. T. Sakuta and Y. Kito, IEEE Trans. on Pl. Sci. PS-8, 29-32 (1980).
10. G. Herzberg, Molecular Spectra and Molecular Structure, I. Spectra of Diatomic Molecules, Van Nostrand Reinhold, New York (1950).
11. W. Hermann, U. Kogelschatz, L. Niemeyer, K. Ragaller and E. Schade, IEEE Trans. on Power App. and Sys. PAS-95, 1165-1176 (1976).
12. J.E. Fitzgerald and D.M. Benenson, ASME J. of Ht. Trans. **97**, Ser. C, 435-441 (1975).
13. W. Hermann, U. Kogelschatz, L. Niemeyer, K. Ragaller and E. Schade, J. of Phys. D: App. Phys. **7**, 1703-1722 (1974).
14. Y.K. Chien and D.M. Benenson, IEEE Trans on Pl. Sci. PS-8, 411-417 (1980).
15. P.W. Schreiber and A.M. Hunter III, Proceedings of the Xth Inter. Conf. on Phen. in Ionized Gases, Oxford, 406 (1971).
16. J.V. Heberlein and E. Pfender, IEEE Trans. on Pl. Sci. PS-5 171-180 (1977).
17. T.L. Eddy, E. Pfender and E.R.G. Eckert, IEEE Trans. on Pl. Sci. PS-1, 31-42 (1973).
18. P.P. Sorokin and J.R. Lankard, IBM J. Res. and Dev. **10**, 162-163 (1966).
19. T.W. Hänsch, Dye Lasers, Springer-Verlag, Berlin (1977).
20. J. Kuhl and G. Marowsky, Opt. Comm. **4**, 125 (1971).
21. R.N. Zare and P.J. Dagdigian, Science **185**, 739-747 (1974).
22. See, for example: C. Kahler and Y.T. Lee, J. Chem. Phys. **73**, 5122-5130 (1980).
23. See, for example: M.L. Lesiecki and W.A. Guillory, J. Chem. Phys. **69**, 4572-4579 (1979).
24. See, for example: M.J. Pellin, R.B. Wright and D.M. Gruen, J. Chem. Phys. **74**, 6448-6457 (1981).
25. J.H. Bechtel, Appl. Opt. **18**, 2100-2106 (1979).
26. See, for example: B.R. Mollow, Phys. Rev. A **12**, 1919-1953 (1975).
27. J.D. Bradshaw, N. Omenetto, G. Zizak, J.N. Bower and J.D. Winefordner, Appl. Opt. **19**, 2709-2716 (1980).
28. J.W. Daily, Appl. Opt. **17**, 1610-1615 (1978).
29. See, for example: Energy Technology Review, Lawrence Livermore Laboratory, March (1979).
30. F.B. Dunning, Laser Focus, 72-76 (May 1978).
31. Laser Photochemistry and Diagnostics, NSF/DOE Workshop Report, (June 1979).
32. J.H. Bechtel, ACS Symposium Series, No. 134, 85-102 (1980).
33. C. Chan and J.W. Daily, Appl. Opt. **19**, 1963-1968 (1980).
34. J. Kopliansky, in Current Interruption in High Voltage Networks, K. Ragaller, Ed., 329-354 Plenum Press, New York (1978).

35. G. Herzberg, Spectroscopic Data for Diatomic Molecules, 4, Van Nostrand Reinhold, New York (1978).
36. T. Amano and E. Hirota, J. Molec. Spect. 45, 417-420 (1973).
37. S.B. Hyder and T.O. Yep, J. Electrochem. Soc. Sol. State Sci. and Tech. 123, 1721-1724 (1976).
38. P.A. Schulz, A.S. Sudbo, D.J. Krajnovich, H.S. Kwok, Y.R. Shen and Y.T. Lee in Ann. Rev. of Phys. Chem. 30, 379-410 (1979).
39. J.D. Lamb and P.W. Schreiber, Aerospace Research Laboratories, Wright-Patterson Air Force Base, Ohio, Report ARL 66-0222 (1966).
40. U. Kogelschatz, Appl. Opt. 13, 1749-1752 (1974).
41. W. Tiemann, Siemens Forschu.-u.Entwickl-Ber. 5, 163-170 (1976).
42. W. Hertz, J. Mentel, W. Tiemann, Siemens Forsch.-u.Entwickl-Ber. 3, 5-12 (1974).
43. U. Kogelschatz and W.R. Schneider, Appl. Opt. 11, 1822-1832 (1972).
44. M. Lapp, C.M. Penney and J.A. Asher, Aerospace Research Laboratories, Wright-Patterson Air Force Base, Ohio, Report ARL 73-0045 (1973).
45. D. Celenti and D.M. Benenson, private communication (1981).
46. M.R. Barrault, N. Collings, G.R. Jones and T.R. Blackburn, University of Liverpool, Liverpool, United Kingdom, Report ULAP-T13 (1973).
47. M.I. Boulos, IEEE Trans. on Pl. Sci. PS-6, 93-106 (1978).
48. J. Lesinski, B. Mizera-Lesinski, J. Jurewicz and M.I. Boulos, 88th AIChE Meeting, Philadelphia, Pennsylvania (1980).